sustainability

MDPI

Article

Modelling of Railway Sleeper Settlement under Cyclic Loading Using a Hysteretic Ballast Contact Model

Elahe Talebiahooie [1,*], Florian Thiery [1,†], Jingjing Meng [2,†], Hans Mattsson [2,†] and Erling Nordlund [2,†] and Matti Rantatalo [1,†]

[1] Division of Operation and Maintenance Engineering, Luleå University of Technology, 97187 Luleå, Sweden; florian.thiery@ltu.se (F.T.); Matti.Rantatalo@ltu.se (M.R.)
[2] Division of Mining and Geotechnical Engineering, Luleå University of Technology, 97187 Luleå, Sweden; jingjing.meng@ltu.se (J.M.); Hans.Mattsson@ltu.se (H.M.); Erling.Nordlund@ltu.se (E.N.)
* Correspondence: elahe.talebiahooiei@ltu.se; Tel.: +46-(0)920-493688
† These authors contributed equally to this work.

Abstract: Ballasted tracks are common in the railway system as a means of providing the necessary support for the sleepers and the rails. To keep them operational, tamping and other maintenance actions are performed based on track geometry measurements. Ballast particle rearrangement, which is caused by train load, is one of the most important factors leading to track degradation. As a result, when planning maintenance, it is vital to predict the behaviour of the ballast under cyclic loading. Since ballast is a granular matter with a nonlinear and discontinuous mechanical behaviour, the discrete element method (DEM) was used in this paper to model the ballast particle rearrangement under cyclic loading. We studied the performance of linear and nonlinear models in simulating the settlement of the sleeper, the lateral deformation of the ballast shoulder and the porosity changes under the sleeper. The models were evaluated based on their ability to mimic the ballast degradation pattern in vertical and lateral direction. The linear contact model and the hysteretic contact model were used in the simulations, and the effect of the friction coefficient and different damping models on the simulations was assessed. An outcome of this study was that a nonlinear model was proposed in which both the linear and the hysteretic contact models are combined. The simulation of the sleeper settlement and the changes in the porosity under the sleeper improved in the proposed nonlinear model, while the computation time required for the proposed model decreased compared to that required for the linear model.

Keywords: ballasted track; linear contact model; hysteretic contact model; cyclic loading; DEM

Citation: Talebiahooie, E.; Thiery, F.; Meng, J.; Mattsson, H.; Nordlund, E.; Rantatalo, M. Modelling of Railway Sleeper Settlement under Cyclic Loading Using a Hysteretic Ballast Contact Model. *Sustainability* **2021**, *13*, 12247. https://doi.org/10.3390/su132112247

Academic Editor: Marinella Silvana Giunta

Received: 12 October 2021
Accepted: 2 November 2021
Published: 6 November 2021

1. Introduction

Ballasted track is composed of two main parts called the superstructure and the substructure. The rails, sleepers and fastening system are the components that form the superstructure, while the substructure is composed of the ballast, sub-ballast and subgrade parts, as shown in Figure 1. The ballast bed rests on a sub-ballast layer, which transmits the stress to the subgrade layer [1].

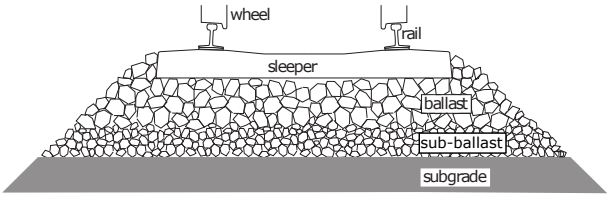

Figure 1. Cross-section view of typical ballasted track. For a more detailed view, see Selig and Waters [2].

Ballast needs frequent maintenance actions such as tamping to retain or restore the track quality and ride comfort, as well as decreasing the probability of catastrophic incidents such as derailment. High track irregularities as the result of insufficient maintenance not only affect the passenger comfort [3] but also deteriorate the vehicle–infrastructure interaction performance [4]. Maintenance planning, simulation of the track–train interaction and derailment risk assessment can be improved by acquiring accurate models of the ballast.

Analytical methods such as the Boussinesq's classical problem [5] and numerical methods such as the finite element method (FEM), the boundary element method (BEM) and the discrete element method (DEM) can be used to simulate the ballast degradation rate. Since the ballast is a granular material which has a nonlinear and discontinuous mechanical behaviour under loading, this makes analytical methods and continuous numerical methods, such as FEM or BEM, which are methods for application to continuous problems, less practical in modelling ballast degradation at the particle level. DEM allows a more detailed study of the ballast in particle level than is often possible in experiments. For instance, the porosity changes in the ballast can be measured using DEM, or as in Chen et al.'s study [6], other parameters such as coordination number or the rotation angle of each particle can be monitored by DEM. Monitoring the force chains during the loading is another positive aspect of performing DEM simulations [7].

In order to develop an accurate DEM-based model for ballast degradation, the effect of different contact models and damping models as well as different parameters such as the shape of the aggregates and the possibility of breakage should be investigated. Lobo and Vallejo [8] showed that the breakage of the ballast aggregates under the sleeper increases the ballast settlement rate. The effect of the aggregates' shape [9] and the occurrence of breakage [10] has already been documented in the literature, but there is still a need for studying the effect of different contact models and damping models on the accuracy of simulations, and this was investigated in the present study.

After developing the DEM model, the parameters of the contact models should be calibrated. Data collected from triaxial tests, shear-box tests, model of a section of the track or experiments performed in railway test facilities are used for the calibration of DEM models. Huang and Tutumluer [11] used the calibrated contact parameters based on the shear box test to simulate fouled ballast degradation under the sleeper.

The majority of the data that is used for the calibration of the DEM models is produced in controlled laboratory conditions which are different from the in situ conditions. In order to improve these models' randomness, different aspects can be added to the models. For instance, random particle orientation or random particle shapes can be considered. Cheng et al. [12] implemented the randomness in the shape of the sand particles in their study. They assigned an existence probability to the pebbles generating the spherical clumps, which were the representative of the sand particles.

In the case of traditional DEM simulations performed on a central processing unit (CPU), the size of the simulated area should be limited to the size of the surroundings of one sleeper, with the ballast layer mainly considered in 3D simulations, and with the number of loading cycles limited to approximately 10^3 cycles [13,14]. Alternatively, the simulation should be performed in 2D [15] with a higher number of loading cycles.

The aim of the present authors was to verify their simulation models using the experimental data obtained by Indraratna et al. [16], since the size of the model in the study by Indraratna et al. [16] was limited to the size of the surroundings of one sleeper, and both the exponential and linear behaviour in the settlement could be seen within the first 10^3 cycles of loading; the simulations in the present study were carried out in 3D, while considering the first 10^3 cycles of loading.

Using DEM instead of FEM to simulate granular matter increases the number of factors that must be modelled correctly in order to achieve reasonable results. For instance, the surface texture (e.g., roughness) of the ballast aggregates is one of the properties that can be represented in the simulation as the friction coefficient in the contact models. In order to

measure the aggregate's texture, Masad and Button [17] introduced the surface parameter as a function of the area of the 2D image of the object after implementing the erosion and dilation technique on the image. Tutumluer et al. [18] improved this surface parameter by using it to create a surface texture index in the University of Illinois Aggregate Image Analyzer (UIAIA). Moaveni et al. [19] upgraded the aggregate image processing algorithms implemented in the UIAIA to facilitate the field image-acquisition and image-processing.

The present study concentrated on improving the accuracy of models to obtain a better fit to the real-life degradation rate pattern in both the vertical and the lateral direction. For instance, the ballast degradation rate follows an exponential behaviour in the vertical direction, right after a tamping intervention or whenever the ballast packing has recently been changed or disturbed. After some cycles of loading on the ballast, the settlement follows a linear pattern. The accuracy of the models proposed in this study was verified based on the previously published studies of Indraratna et al. [16] and Song et al. [20].

Even though the contact model plays a major role in DEM simulations, the effect of different contact models in the simulation of ballast degradation had not been investigated thoroughly prior to the present study. Hence, the effect of two different contact models and three different damping models were investigated in the present study.

2. Ballast Degradation Model

In this study, the experimental data from laboratory tests conducted by Indraratna et al. [16] were used to verify the numerical models presented in this section. The PFC3D (Particle Flow Code for 3D) software was used for the simulations, and the results were compared with the simulation results of Chen et al. [13].

Indraratna et al. [16] used fresh latite basalt with an average particle size of 35 mm and a uniformity coefficient of 1.87 in the large-scale process simulation test (PST) apparatus at the University of Wollongong to measure the vertical and horizontal degradation of a ballast layer under high-frequency cyclic loading. The particle size distribution of the ballast is available in Indraratna et al. [16].

A layer of a sand–gravel mixture with a thickness of 150 mm was used to represent the sub-ballast layer. The ballast layer was compacted up to a density of 1550 kg/m^3.

A schematic diagram of the PST apparatus and the area of the track simulated in the tests in the laboratory is shown in Figure 2. All the side walls of the PST were fixed, except for five plates, which are shown as movable walls in Figure 2.

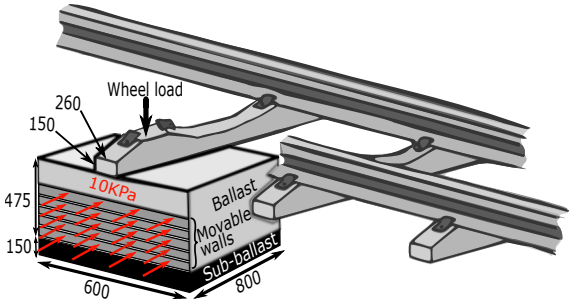

Figure 2. The section of track simulated, its boundary conditions and the large-scale PST apparatus at the University of Wollongong [16]. The dimensions are in mm. The sub-ballast section shown here was omitted in the simulations.

The settlement of the ballast aggregates had an exponential shape at the beginning of the loading and transitioned towards a linear behaviour for a large number of cycles, as shown by Indraratna et al. [16].

Selecting the most appropriate contact model among the different compliant contact models which have been proposed during the past few decades is a challenging and important issue to be addressed [21]. The linear contact model with bonding used in the simulations carried out by Chen et al. [13] do not show the exponential part of the

settlement entirely. Hence, the present study tried to improve the simulation results by investigating the implementation of other contact models. Accordingly, the linear contact model and the hysteretic contact model were tested, and the results obtained were compared with the modified results mentioned in Chen et al. [13]. In their work, the ballast aggregates were simulated with two-ball clumps, as shown in Figure 3. In the simulations performed in the present study, the same particle shape and size were selected as had been used in Chen et al. [13]. One of the limitations of using two-pebble clumps is the lack of angularity, while high angularity is one of the properties of the ballast aggregates.

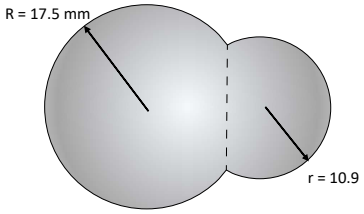

Figure 3. Two-ball clumps used in [13] to represent the ballast aggregates.

In the PFC, the first step is to create a domain that will contain the mechanical model. This domain dictates the behaviour that the model components should follow when they reach the domain boundaries by destroying, stopping, reflecting, or reinserting them. In our case, all the domain boundary conditions were set to "stop" to monitor the particles' location in the case of instability during the simulation process.

After creating the domain, the walls of the model and the sleeper were created. In the present study, the movable walls on the shoulder side of the model had a 1 mm gap in between. The dimensions of each movable wall were 600 × 64 mm and the dimensions of the section of the wall above the movable walls were 600 × 150 mm, while the sleeper's dimensions were 150 × 260 × 800 mm as described in Figure 2.

In the packing step, all the walls are fixed. After packing the particles, during the preloading and loading steps, the sleeper can only move vertically, while the movable walls, which represent the track's shoulder, can only move horizontally.

The packing step is important and can be carried out in different ways. In the present study, since the sleeper was blocking the top of the model, non-overlapping balls with a radius of 11.5625 mm were generated by hexagonal packing in the space between the sleeper and the walls of the model with a certain gap, as shown in Figure 4. In order to let the particles expand without penetrating the walls, the top of the model and the space around the sleeper were blocked temporarily, as shown in Figure 4.

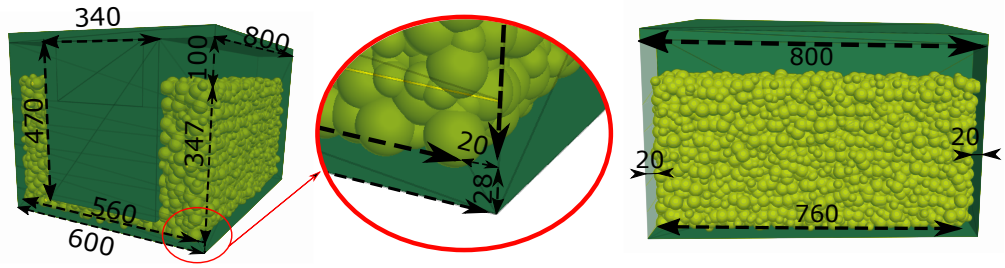

Figure 4. Front and side view of the model during the packing step (after replacing the balls with clumps).

The balls were expanded to obtain a radius of 18.5 mm. A sub-routine was employed to replace each of these balls with clumps of random orientations. After replacing the balls with the clumps, the model was cycled while the friction coefficient was set to zero in order to decrease the overlap between the clumps. Then, the two extra boxes in the model (the one around the sleeper and the one on the top of the model) were deleted, and

under a gravity of -300 m/s^2 and a friction coefficient of 0.5 between the clumps and walls, the model was cycled until it became stable. Finally, the extra clumps which came out of the box were deleted. In this step, the gravity was changed slowly from -300 m/s^2 to -9.81 m/s^2 and the friction coefficient was set to the final value, which was used in the preloading and loading steps. The model at the end of the packing step is shown in Figure 5.

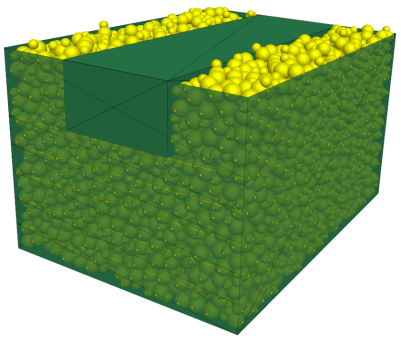

Figure 5. The model before the preloading step.

In order to eliminate the effect of the initial condition on the results of the simulation, in the preloading step, the servo-mechanics used to produce the vertical stress on the sleeper were equal to 50 kPa, and those used to create the stress on the lateral walls were equal to 10 kPa. Then, the cumulative displacement of the walls and sleeper during preloading was set to 0.0.

In the loading step (Figure 6), 1000 cycles of loading with a frequency of 20 Hz, a minimum stress of 50 kPa and a maximum stress of 460 kPa were applied on the sleeper by the servo-mechanism, while a confining pressure of 10 kPa was applied on the movable walls.

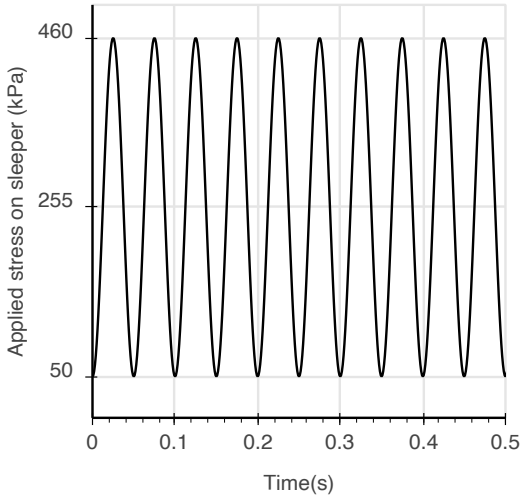

Figure 6. Vertical stress applied on sleeper.

2.1. Linear Contact Model

The linear contact model in the particle flow code (PFC) has two groups of components, forming a linear part and a dashpot part. The moment in the contact area is not transmitted between particles, and the linear part only tolerates compression force. The dissipation of energy can be a result of strain, dashpots or the slipping of the particles.

The energy dissipation during impact in low-speed collisions, where the velocity of the collision is significantly lower than the speed of the internal pressure waves in the colliding bodies, is due to the conversion of kinetic energy to internal vibrational energy

which is eventually damped out by the material [22]. The damping added in the models is a tool to mimic this phenomenon.

The version of the linear contact model which was used in this study is shown in Figure 7. The formulation of the linear contact model based on our selection of parameters is explained in this section as follows.

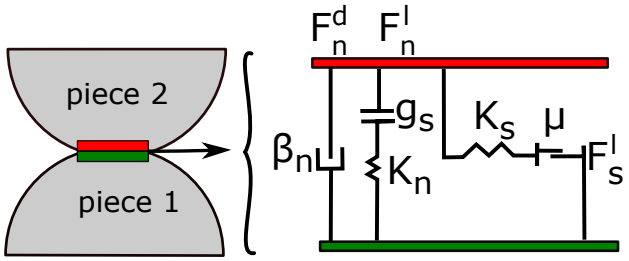

Figure 7. Behaviour and rheological components of the linear contact model used in the simulations based on [23].

In each timestep of the simulation, the linear normal force, the linear shear force and the dashpot normal force are updated, respectively. Since the shear damping coefficient was set to 0.0 in this study, the dashpot shear force will not be discussed here. Equation (1) to Equation (7) are the modified version of the linear contact model equations from PFC documentation [23].

The linear normal force is calculated using Equation (1). With this formulation, there is no contact tension, and the only force which is calculated is compression. The surface gap, g_s, is the indentation in the contact and k_n is the normal stiffness.

$$F_n^l = \begin{cases} k_n g_s & \text{if} \quad g_s < 0 \\ 0 & \text{otherwise} \end{cases} \tag{1}$$

After computing the linear normal force, the trial linear shear force ($\mathbf{F_s^*}$) is calculated using Equation (2). The linear normal force is a function of the linear shear force at the beginning of the timestep $\left(\mathbf{F_s^l}\right)_o$, the relative shear-displacement increment ($\Delta\boldsymbol{\delta}_\mathbf{s}$) and the shear stiffness (k_s).

$$\mathbf{F_s^*} = \left(\mathbf{F_s^l}\right)_o - k_s \Delta\boldsymbol{\delta}_\mathbf{s} \tag{2}$$

During the timestep, the surface gap can change from negative to positive values, which indicates that two surfaces without contact at the beginning of the timestep can reach each other. In this case, the $\Delta\boldsymbol{\delta}_\mathbf{s}$ is updated using Equation (3), and then the updated value is used in Equation (2) to calculate $\mathbf{F_s^*}$.

$$\Delta\boldsymbol{\delta}_\mathbf{s} := \frac{g_s}{g_s - (g_s)_o} \Delta\boldsymbol{\delta}_\mathbf{s} \tag{3}$$

In order to determine whether slipping is happening at the contact point, the shear strength (F_s^μ) is computed based on the friction coefficient (μ) and F_n^l in Equation (4).

$$F_s^\mu = -\mu F_n^l. \tag{4}$$

If $\mathbf{F_s^*}$ exceeds the shear strength, slipping is happening during the contact, and the value of the linear shear force will be equal to the shear strength, as shown in Equation (5).

$$\mathbf{F_s^l} = \begin{cases} \mathbf{F_s^*} & \text{if} \quad \|\mathbf{F_s^*}\| \le F_s^\mu \\ F_s^\mu \left(\mathbf{F_s^*} / \|\mathbf{F_s^*}\|\right) & \text{otherwise.} \end{cases} \tag{5}$$

The last step in the contact force calculation is the evaluation of the dashpot normal force (F_n^d), which is updated using Equation (6), where m is the mass calculated by Equation (7) and $\dot{\delta}_n$ is the relative normal translation velocity of the pieces in contact.

$$F_n^d = \left(2\beta_n\sqrt{mk_n}\right)\dot{\delta}_n \tag{6}$$

$$m = \begin{cases} \dfrac{m^{(1)}m^{(2)}}{m^{(1)}+m^{(2)}} & \text{for ball-ball contacts} \\ m^{(1)} & \text{for ball-facet contacts} \end{cases} \tag{7}$$

More detailed information about the full linear contact model formulation and parameters can be found in the PFC documentation [23].

2.2. Hysteretic Contact Model

The hysteretic contact model in the PFC consists of a combination of the Hertzian contact theory [24], which is applicable in cases where the normal force in a contact is varying and the tangential force is zero as well as in the theory of Mindlin and Deresiewicz [25], which includes a dashpot group in the normal direction.

The hysteretic contact model does not transmit momentum, similarly to the linear contact model. The forces during contact are updated in the following order:

1. The hertz model normal force (F_n^h).
2. The hertz model shear force (F_s^h).
3. The dashpot normal force (F_n^d).

The version of the hysteretic contact model which was used in this paper is shown in Figure 8.

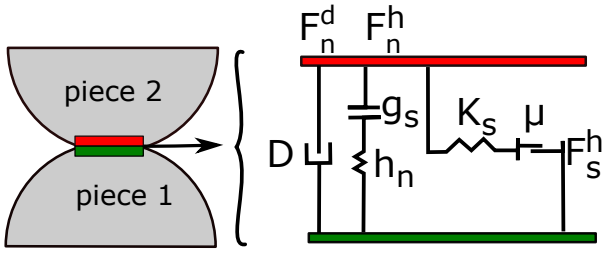

Figure 8. Behaviour and rheological components of the hysteretic contact model used in the simulations based on [23].

The formulation of the hysteretic contact model based on our selection of parameters is explained in this section as follows. Equation (8) to Equation (16) are the modified version of the hysteretic contact model equations from PFC documentation [23]. The hertz model normal force is calculated using Equation (8). F_n^h depends on the particles' shear modulus (G), the Poisson's ratio (ν) and the effective radius of the contact ($\bar{R}$).

$$F_n^h = -\frac{2G\sqrt{2\bar{R}}}{3(1-\nu)}|g_s|^{1.5} = -h_n|g_s|^{1.5} \tag{8}$$

In our simulations, the contact model for the particle–particle contact in the nonlinear model was the hysteretic contact model, but the contact between the walls and the particles was defined with the linear contact model, so $\bar{R}$ could be calculated based on the radius of the particles in Equation (9).

$$\frac{1}{\bar{R}} = \frac{1}{2}\left(\frac{1}{R^{(1)}} + \frac{1}{R^{(2)}}\right) \tag{9}$$

After computing the Hertz model normal force, $\mathbf{F_s^h}$ is computed with the same procedure as that used in the computation of the linear shear force, and an assessment is made of the slip occurrence in the contact (Equations (10) and (11)).

$$\mathbf{F_s^*} = (\mathbf{F_s^h})_0 + k_s \Delta \boldsymbol{\delta}_\mathbf{s} \tag{10}$$

The shear stiffness depends on the mechanical characteristics of the particles and the indentation of the contact, as in Equation (11).

$$k_s = \frac{-2(G)\sqrt{2|g_s|\bar{R}}}{2-\nu} \tag{11}$$

The shear strength is computed by Equation (12) in order to determine whether the slip is happening in the contact or not.

$$F_s^\mu = \mu F_n^h. \tag{12}$$

If the F_s^* exceeds the F_s^μ, then slip is happening in the contact. $\mathbf{F_s^h}$ is determined by Equation (13).

$$\mathbf{F_s^h} = \begin{cases} \mathbf{F_s^*}, & \|\mathbf{F_s^*}\| \le F_s^\mu \\ F_s^\mu(\mathbf{F_s^*}/\|\mathbf{F_s^*}\|), & \text{otherwise.} \end{cases} \tag{13}$$

The hysteretic contact model in the PFC [23] contains a damping force ($\mathbf{F^d}$) only in the normal direction, as in Equation (14).

$$\mathbf{F^d} = -F_n^d \hat{\mathbf{n}}_\mathbf{c} \tag{14}$$

The normal damping force depends on the ratio of the relative normal translation velocity ($\dot{\delta}_n$) to the initial normal impact velocity ($\dot{\delta}_n^{(-)}$), the damping factor (D) and F_n^h, as in Equation (15).

$$F_n^d = DF_n^h \frac{\dot{\delta}_n}{\dot{\delta}_n^{(-)}} \tag{15}$$

The damping factors for the different damping modes can be found in Equation (16) and Figure (9).

$$D = \begin{cases} \dfrac{1-e_n^2}{e_n} & \text{for} \quad M_d = 0 \\ \dfrac{3(1-e_n^2)}{4} & \text{for} \quad M_d = 1 \\ \dfrac{3(1-e_n^2)e^{2(1-e_n)}}{4} & \text{for} \quad M_d = 2 \end{cases} \tag{16}$$

As Machado et al. stated [21], the Hertzian contact model has been the main tool for modelling contact interactions over the past few decades, but it is not appropriate for most impacts regarding the amount of energy dissipated during the impact. Hence, adding a damping term can help solve this problem.

By using the hysteretic contact model, three different built-in formulations are available to facilitate the simulation of the energy dissipated during impact. All of these three built-in models are based on the point-contact perspective. The mode $M_d = 0$ in the PFC is based on the work of Gonthier et al. [22]. In this model, for higher restitution coefficients, the damping in the compression and restitution phase is symmetrical, and a decrease in the restitution coefficient will increase the dissipated energy in the compression phase [22].

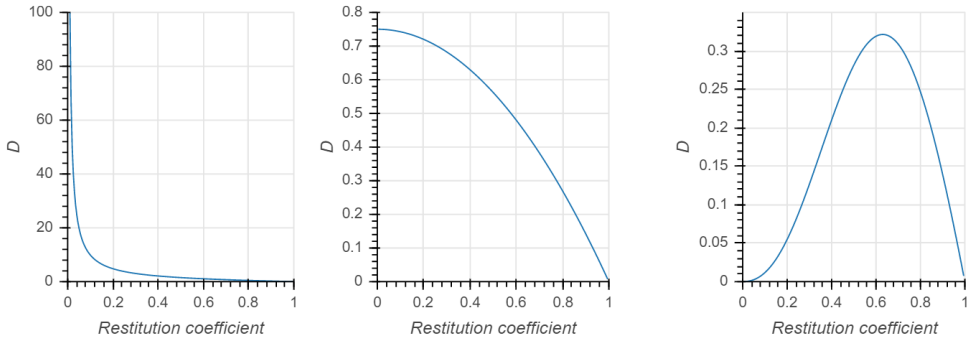

(**a**) (**b**) (**c**)

Figure 9. Comparison between the three different damping factors in the hysteretic contact model. (**a**) $M_d = 0$, (**b**) $M_d = 1$, (**c**) $M_d = 2$.

The mode $M_d = 1$ is based on the work of Lankarani et al. [26] and is suitable for models in which the amount of dissipated energy is relatively small compared to the maximum absorbed elastic energy [21]. Finally, the mode $M_d = 2$ is based on the work of Zhiying et al. [27].

3. Results and Discussion

Based on the contact models described above, one linear and one nonlinear model were generated in the present study. In the linear model, the linear contact model was used for all the implemented contacts, while in the nonlinear model, both the hysteretic and the linear contact models were used. The results from the simulations were compared with the experimental results of Indraratna et al. [16] and the simulation results of Chen et al. [13].

The density of the particles, the initial values of k_s and k_n in the calibration process of the models, was determined based on Chen et al. [13]. During the calibration, the friction coefficient was adjusted for both the linear model and the nonlinear model. In the nonlinear model, k_n for the wall–particle contacts was calibrated from 10^9 N/m to 10^8 N/m.

The Young's modulus of the scaled basaltic rock masses is between 10 GPa to 40 GPa, with Poisson's ratio of 0.3 [28]. Therefore, the shear modulus is varying between 3.85 GPa and 15.38 GPa. The Poisson's ratio value in the nonlinear model was 0.3. To decrease the computation time, smaller values of the shear modulus are normally used compared to the shear modulus of the ballast in the experiments. During the calibration of the nonlinear model, the shear modulus was varying from 21 MPa to 250 MPa, similar to the parametric study of Suhr and Six [29]. Based on the calibration process, a shear modulus of 35 MPa was selected for the calibrated nonlinear model.

The contact parameters used in the linear model and nonlinear model of the present study and the simulation of Chen et al. are listed in Tables 1–3, respectively.

Table 1. Parameter values in the linear model.

Parameters	Values	Unit
ine Density of particles	2600	kg/m^3
Normal stiffness of particle–particle	10^8	N/m
Shear stiffness of particle–particle/particle–wall	10^8	N/m
Normal stiffness of wall–particle	10^9	N/m
Friction coefficient of particle–particle/particle–wall	0.7, 0.8, 0.9	-
Damping coefficient of particle–particle/particle–wall	0	-
Initial porosity under sleeper	≈0.35	-
Number of particles	4583	clump
Time step	≈29 $\times 10^{-7}$	s

Table 2. Parameter values in the nonlinear model.

Parameter	Value	Unit
ine Density of particles	2600	kg/m^3
Shear modulus of particle–particle	35	MPa
Poisson ratio of particle–particle	0.3	-
Friction coefficient of particle–particle	0.75	-
Shear stiffness of wall–particle	10^8	N/m
Normal stiffness of wall–particle	10^8	N/m
Friction coefficient of wall–particle	0.9	-
Normal damping ratio of wall–particle	0.06	-
Normal restitution coefficient of particle–particle	0, 0.3, 0.6, 0.9, 1.0	-
Initial porosity under sleeper	≈0.35	-
Number of particles	4429	clumps
Time step	$\approx 63 \times 10^{-7}$	s

Table 3. Parameter values in Chen et al. [13].

Parameter	Values	Unit
ine Density of particles	2600	kg/m^3
Normal stiffness of particles	10^8	N/m
Shear stiffness of particles	10^8	N/m
Normal stiffness of wall–particle	10^9	N/m
Friction coefficient of particle–particle/particle–wall	0.6	-
Parallel bond normal stiffness	4×10^9	N/m
Parallel bond shear stiffness	5×10^6	N/m
Parallel bond normal strength	3×10^7	N
Parallel bond shear strength	3×10^7	N

3.1. Settlement and Lateral Deformation

In the presented linear model, the damping coefficient was set to 0.0 so that the energy dissipation from the dashpot component in the contact model was omitted. The linear model was simplified, and the critical damping ratio in the shear and the normal directions were set as equal to zero.

The sensitivity of the linear model to the friction coefficient was investigated to evaluate its effect on both the settlement and the lateral deformation, as seen in Figure 10. The results of the simulations were compared with the experimental results of Indraratna et al. [16] and the simulation results of Chen et al. [13].

For the settlement, the linear model showed a good agreement with the simulation results from Chen et al. [13], although neither their linear model with bonding between particles (the Linearpbond contact model in the PFC [23]) nor our linear model were able to display the same settlement characteristics as the experimental results of Indraratna et al. [16] at the beginning of the loading.

After 1000 cycles of loading, the linear contact model showed better results compared to the linear parallel bond contact model (the Linearpbond contact model in the PFC [23]) with regard to the lateral deformation. However, in the first cycle, the results from Chen et al. [13] exhibited better agreement with the experimental data [16]. The results of the first cycle depend greatly on the packing of the particles. The number of clumps in the simulations of Chen et al. [13] was equal to 7583, and with regard to the size of the model, the particles were completely packed, which increased the initial inter-particle compression force.

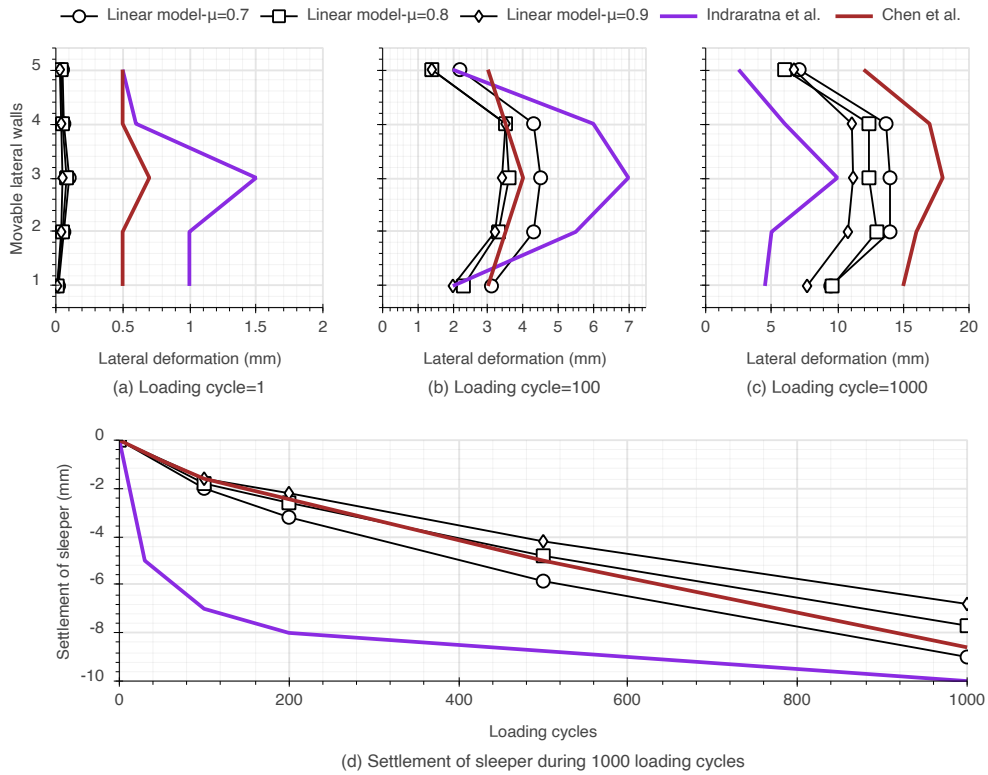

Figure 10. Comparison of the lateral deformation of the movable lateral walls and the settlement of the sleeper obtained with the linear model in this study, in the simulation of Chen et al. [13] and in the experiments of Indraratna et al. [16].

Even if the linear model was able to mimic the lateral deformation after 100 cycles and 1000 cycles of loading, it was not able to mimic either the exponential behaviour of the settlement at the beginning of the loading or the lateral deformation after one cycle of loading. Hence, the nonlinear model was generated to improve the simulations in this regard.

In the nonlinear model, the hysteretic contact model was used for the particle–particle contacts, while the linear contact model was used for the particle–wall contacts. This combination of contact models was selected because it provided a faster convergence of the simulations at the same time as better results were achieved with this combination with regard to the deformation and the settlement.

A sensitivity analysis was performed on the built-in damping models and different damping factor values in order to find the best damping model and damping factor for our simulations.The settlement for the different damping modes is shown in Figure 11. Since most of the energy in the experiment was damped in the compression phase, the model created by Gonthier et al. [22] was expected to show better agreement with the experimental results, especially for smaller values of the restitution coefficient. Contrary to our expectations, the results from Lankarani et al. [26] showed better agreement with the experimental results in total, as shown in Figure 11b. Machado et al., in their study on the evolution of the Hertz contact theory [21], mentioned that the model created by Lankarani et al. was satisfactory for general mechanical contacts, and this statement is in agreement with our results.

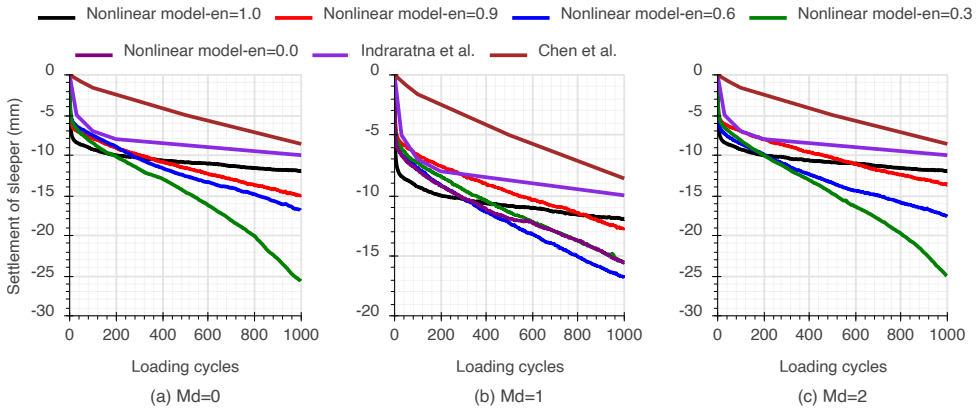

Figure 11. Comparison of the settlement of the sleeper obtained with the nonlinear model in this study, in the simulations of Chen et al. [13] and in the experiments of Indraratna et al. [16].

The lateral deformation for the different damping modes is shown in Figure 12. After the first cycle of loading, the lateral deformation of the movable lateral walls for $M_d = 0$ was much greater than that obtained in the experiments of Indraratna et al., while the corresponding lateral deformation for $M_d = 1$ and $M_d = 2$ showed better agreement in comparison. Similarly, concerning the settlement, the results for $M_d = 1$ with $e_n = 0$ show good agreement with the experimental Indraratna et al. [16].

The results for all three different damping modes for the lateral deformation after 100 cycles of loading converged to similar values (Figure 12), even if, after just one cycle of loading, the lateral deformation for $M_d = 0$, was about twice that for the other two damping modes.

The results for the lateral deformation of the movable walls after 1000 cycles of loading show that $e_n = 1$ gives the best agreement with the results for the corresponding lateral deformation obtained in the experiments performed by Indraratna et al. [16]. In addition, the results for the corresponding lateral deformation for $M_d = 1$ show the best agreement with the corresponding results for $M_d = 0$ and $M_d = 2$ (Figure 12).

The settlement results for both $M_d = 0$ and $M_d = 2$ models are giving increased deviation from the experimental results with a decreasing e_n. For this reason, the results for $e_n = 0$ for these two damping models are not included in this paper. On the other hand, the model with $M_d = 1$ and $e_n = 0$ showed better results than the model with $M_d = 1$ and $e_n = 0.3$.

Although this sensitivity analysis led to the conclusion that the best result was obtained with $e_n = 1$, there is also the possibility that a change in other parameters such as the shear modulus and the friction coefficient with $e_n = 1$ for $M_d = 1$ might improve the results. Based on the sensitivity analysis, it can be concluded that the best agreement with the experimental results obtained by Indraratna et al. [16] and the simulation results of Chen et al. [13] was obtained with $e_n = 1$.

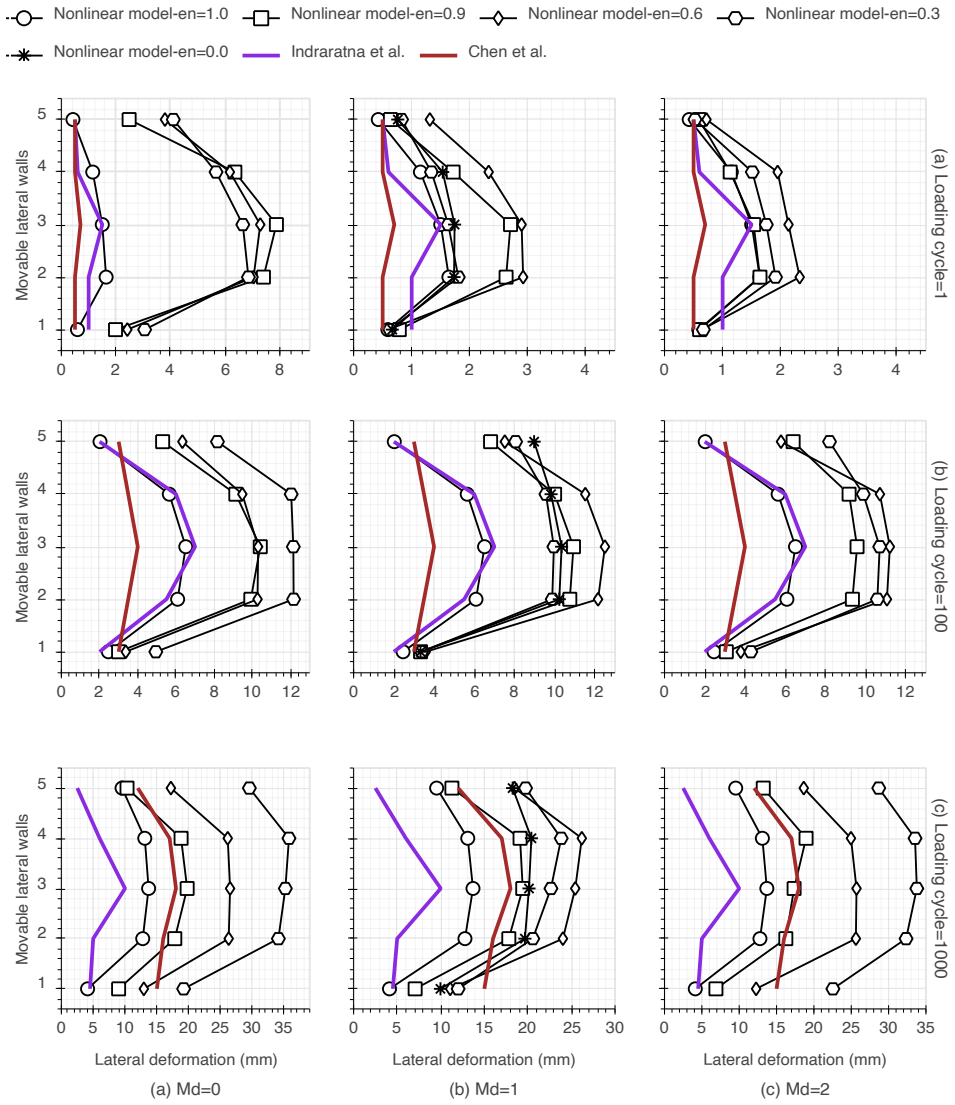

Figure 12. Comparison of the lateral deformation of the movable lateral walls obtained with the nonlinear model in this study, in the simulation of Chen et al. [13] and in the experiments of Indraratna et al. [16].

3.2. Porosity Analysis

The porosity of the ballast layer affects the water drainage capacity of the track. The capability of the linear model and the nonlinear model to represent the changes in the porosity during loading was monitored. Under the sleeper, three spheres with a radius of 134 mm were used to determine the porosity of the ballast during the loading process. These measurement spheres and the porosity changes of the linear model and the nonlinear model are shown in Figure 13.

The range of changes in the porosity for the linear model is smaller than the corresponding range for the nonlinear model. A possible reason for this may be the approach that was used to produce the nonlinear model. In order that the packing of the models would be as similar as possible, the nonlinear model was produced based on the packed linear model by just changing the contact models before the preloading step. To obtain a stable model, after changing the contact models, the nonlinear model was cycled until it reached stability. During this process, 154 clumps that came out of the box were deleted before the start of preloading.

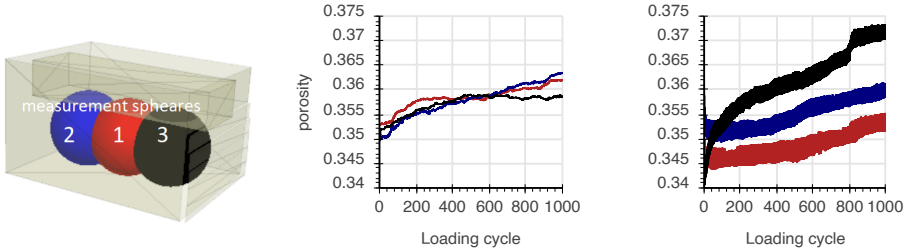

(**a**) (**b**) (**c**)

Figure 13. Comparison of the porosity changes in the measurement spheres under the sleeper for the linear and nonlinear models during loading. (**a**) Measurement spheres, (**b**) Linear model, (**c**) Nonlinear model.

Even if the number of clumps in the nonlinear model is smaller than that in the linear model, the porosity of the nonlinear model still has smaller values at the beginning of the loading because of the hysteretic contact model. At the beginning of the loading for particles with hysteretic contact model, the indentation is much smaller compared to that in the later cycles of loading. A smaller amount of indentation results in a smaller value for the particle–particle stiffness, meaning that the particles will resist less to the compression. Consequently, in the preloading step for the nonlinear model, the movable walls move inside the box, and this results in a sudden drop in the porosity compared to the corresponding porosity level in the linear model. The slopes of the porosity in measurement sphere 1 and 2 in both models are similar, but the porosity in measurement sphere 3 is steeper. This behaviour can be caused by F_n^l, which is lower in the nonlinear model than in the linear model.

The pattern of the final porosity in the nonlinear model agrees with the results from Song et al. [20], which implies that the largest amount of porosity occurs in the shoulder of the track (measurement sphere 3), and the smallest amount of porosity occurs in the section under the rail seat (measurement sphere 1).

4. Concluding Remarks

In this study, the effect of implementing a linear contact model and a hysteretic contact model as well as the effect of using three different damping models on the accuracy of the ballast degradation simulation was assessed.

A linear model and a nonlinear model based on a selection of contact models for the particle–particle contacts and particle–wall contacts were investigated. In the linear model, all the contact models were linear contact models without damping. In the investigated nonlinear model, the models for the particle–particle contacts were hysteretic contact models, and those for the the wall–particle contacts were linear contact models.

The performance of the studied models was assessed based on the settlement of the ballast, the lateral deformation of the lateral movable walls, the porosity changes in the model and the computation time.

The nonlinear model showed a better performance in simulating the exponential shape of the settlement of the sleeper, as well as the slope of the final linear part of the settlement curve.

The main difference in the settlement between the simulation results and the experimental results is a fairly constant shift in the vertical direction of the simulation results compared to the experimental results. The reason for this could be the unknown initial condition of the experimental setup and the difference in the packing of the ballast between the simulations and the experiments.

The lateral deformation of the movable lateral walls was monitored after one cycle, 100 cycles and 1000 cycles of loading. The nonlinear model showed better results in simulating the lateral deformation of the movable walls after one cycle and 100 cycles of loading compared to the linear model. The accuracy for the lateral deformation of the

movable lateral walls after 1000 cycles of loading is comparable in both the linear and the nonlinear models.

The pattern of the porosity changes obtained with the nonlinear model was better than that obtained with the linear model, and the computation time required by the former model was shorter than that required for the latter.

A sensitivity analysis was performed on the built-in damping models in the hysteretic contact model used in the nonlinear model. The damping model created by Lankarani et al. [26] ($M_d = 1$) showed more promising results than the damping models created by Gonthier et al. [22] and Zhiying et al. [27]. Decreasing the restitution coefficient increases both the lateral and the settlement in the models with the damping models created by Gonthier et al. [22] and Zhiying et al. [27], and the same trend was observed for models with the damping model created by Lankarani et al. [26] up to a restitution coefficient of 0.6, after which the trend was reversed.

The breakage of the aggregates and the real shape of the ballast aggregates were not considered in this study. The long computation time for each simulation limited the number of simulated loading cycles.

Author Contributions: Conceptualization, E.T., F.T., J.M., H.M. and M.R.; methodology, E.T., F.T., J.M., H.M. and M.R.; software, E.T., J.M., F.T. and E.N.; validation, E.T., F.T., J.M., H.M. and M.R.; formal analysis, E.T.; investigation, E.T.; resources, E.N.; data curation, E.T.; writing—original draft preparation, E.T.; writing—review and editing, E.T., F.T., J.M., H.M., E.N. and M.R.; visualization, E.T. and F.T.; supervision, M.R. All authors have read and agreed to the published version of the manuscript.

Funding: This research funded by Luleå Railway Research Centre (JVTC).

Institutional Review Board Statement: Not applicable.

Informed Consent Statement: Not applicable.

Data Availability Statement: The data presented in this study are available on request from the corresponding author.

Conflicts of Interest: The authors declare no conflict of interest..

References

1. Esveld, C. *Modern Railway Track*; MRT-Productions: Zaltbomme, The Netherlands, 2001.
2. Selig, E.T.; Waters, J.M. *Track Geotechnology and Substructure Management*; Thomas Telford Services Ltd.: London, UK, 1994.
3. Lewis, T.; Jiang, J.Z.; Neild, S.; Gong, C.; Iwnicki, S. Using an inerter-based suspension to improve both passenger comfort and track wear in railway vehicles. *Veh. Syst. Dyn.* **2020**, *58*, 472–493. [CrossRef]
4. Song, Y.; Wang, Z.; Liu, Z.; Wang, R. A spatial coupling model to study dynamic performance of pantograph-catenary with vehicle-track excitation. *Mech. Syst. Signal Process.* **2021**, *151*, 107336. [CrossRef]
5. Selvadurai, A. The analytical method in geomechanics. *Appl. Mech. Rev.* **2007**, *60*, 87–106. [CrossRef]
6. Chen, J.; Indraratna, B.; Vinod, J.S.; Ngo, N.T.; Gao, R.; Liu, Y. Stress-dilatancy behaviour of fouled ballast: Experiments and DEM modelling. *Granul. Matter* **2021**, *23*, 90. [CrossRef]
7. Li, H.; McDowell, G. Discrete element modelling of two-layered ballast in a box test. *Granul. Matter* **2020**, *22*, 1–14. [CrossRef]
8. Lobo-Guerrero, S.; Vallejo, L.E. Discrete element method analysis of railtrack ballast degradation during cyclic loading. *Granul. Matter* **2006**, *8*, 195. [CrossRef]
9. Guo, Y.; Zhao, C.; Markine, V.; Shi, C.; Jing, G.; Zhai, W. Discrete element modelling of railway ballast performance considering particle shape and rolling resistance. *Railw. Eng. Sci.* **2020**, *28*, 382–407. [CrossRef]
10. Hossain, Z.; Indraratna, B.; Darve, F.; Thakur, P. DEM analysis of angular ballast breakage under cyclic loading. *Geomech. Geoengin.* **2007**, *2*, 175–181. [CrossRef]
11. Huang, H.; Tutumluer, E. Discrete element modeling for fouled railroad ballast. *Constr. Build. Mater.* **2011**, *25*, 3306–3312. [CrossRef]
12. Cheng, Y.; Nakata, Y.; Bolton, M.D. Discrete element simulation of crushable soil. *Geotechnique* **2003**, *53*, 633–641. [CrossRef]
13. Chen, C.; Indraratna, B.; McDowell, G.; Rujikiatkamjorn, C. Discrete element modelling of lateral displacement of a granular assembly under cyclic loading. *Comput. Geotech.* **2015**, *69*, 474–484. [CrossRef]
14. Mishra, D.; Qian, Y.; Huang, H.; Tutumluer, E. An integrated approach to dynamic analysis of railroad track transitions behavior. *Transp. Geotech.* **2014**, *1*, 188–200. [CrossRef]

15. Indraratna, B.; Nimbalkar, S.S.; Ngo, N.T.; Neville, T. Performance improvement of rail track substructure using artificial inclusions–Experimental and numerical studies. *Transp. Geotech.* **2016**, *8*, 69–85. [CrossRef]
16. Indraratna, B.; Hussaini, S.K.K.; Vinod, J. The lateral displacement response of geogrid-reinforced ballast under cyclic loading. *Geotext. Geomembr.* **2013**, *39*, 20–29. [CrossRef]
17. Masad, E.; Button, J.W. Unified imaging approach for measuring aggregate angularity and texture. *Comput.-Aided Civ. Infrastruct. Eng.* **2000**, *15*, 273–280. [CrossRef]
18. Tutumluer, E.; Huang, H.; Hashash, Y.; Ghaboussi, J. Aggregate shape effects on ballast tamping and railroad track lateral stability. In Proceedings of the AREMA Annual Conference, Louisville, Kentucky, 17–20 September 2006; pp. 17–20.
19. Moaveni, M.; Wang, S.; Hart, J.M.; Tutumluer, E.; Ahuja, N. Evaluation of aggregate size and shape by means of segmentation techniques and aggregate image processing algorithms. *Transp. Res. Rec.* **2013**, *2335*, 50–59. [CrossRef]
20. Song, W.; Huang, B.; Shu, X.; Stránskỳ, J.; Wu, H. Interaction between railroad ballast and sleeper: A DEM-FEM approach. *Int. J. Geomech.* **2019**, *19*, 04019030. [CrossRef]
21. Machado, M.; Moreira, P.; Flores, P.; Lankarani, H.M. Compliant contact force models in multibody dynamics: Evolution of the Hertz contact theory. *Mech. Mach. Theory* **2012**, *53*, 99–121. [CrossRef]
22. Gonthier, Y. Contact Dynamics Modelling for Robotic Task Simulation. Ph.D. Thesis, Systems Design Engineering, University of Waterloo, Waterloo, ON, USA, 2007.
23. Itasca Consulting Group, Inc. *PFC—Particle Flow Code, Version 6.0*; Itasca: Minneapolis, MN, USA, 2018.
24. Hertz, H. Ueber die Berührung fester elastischer Körper. *J. Die Reine Angew. Math.* **1882**, *1882*, 156–171.
25. Mindlin, R.D. Elastic spheres in contact under varying oblique forces. *Appl. Mech.* **1953**, *20*, 327–344. [CrossRef]
26. Lankarani, H.M.; Nikravesh, P.E. A contact force model with hysteresis damping for impact analysis of multibody systems. *J. Mech. Des.* **1990**, *112*, 369–376. [CrossRef]
27. Zhiying, Q.; Qishao, L. Analysis of impact process based on restitution coefficient. *J. Dyn. Control* **2006**, *4*, 294–298.
28. Schultz, R.A. Limits on strength and deformation properties of jointed basaltic rock masses. *Rock Mech. Rock Eng.* **1995**, *28*, 1–15. [CrossRef]
29. Suhr, B.; Six, K. Parametrisation of a DEM model for railway ballast under different load cases. *Granul. Matter* **2017**, *19*, 64. [CrossRef] [PubMed]